

## Article

# Investigation of the Impact of Fault Characteristics on the Cost-Effectiveness of Doubly Fed Induction Generator-Based Wind Systems in Withstanding Low-Voltage Ride-Through

Tarek Kandil

School of Engineering and Technology, Western Carolina University, Cullowhee, NC 28723, USA; thassankandil@wcu.edu; Tel.: +1-912-486-4255

**Abstract:** Wind farms utilizing doubly fed induction generators (DFIGs) can have a significant impact on the stability of power networks as both the stator and rotor of the DFIG are linked to the grid, which can result in excessive overcurrent and overvoltage in the event of a grid fault and can activate the protective mechanism, leading to the disconnection of the WF and generating instability in the system. One term that is often mentioned in the literature is low-voltage ride-through (LVRT) capability, which is crucial to the stability of microgrids (MGs). To handle LVRT, advanced protection schemes or supporting devices are required. In addition, MGs must comply with the operational limits imposed by different countries for LVRT. Therefore, numerous solutions for improving LVRT have been proposed, including external approaches that are expensive to adopt and internal procedures that provide economic gains but are more difficult to apply. Consequently, to help lower the cost of installing WFs, the study investigates how fault characteristics affect MGs' ability to meet grid LVRT code requirements or even choose the right code to be used. It also aims to give a clear understanding of how fault characteristics affect the grid's behavior during different types of faults, which will be helpful in choosing the best LVRT-enhancing method or device and for determining the optimal ratings for these devices, and thus reduce the cost of installation. The study offers case studies and simulations using Matlab 2024/Simulink, which could help engineers to ensure reliable grid integration of renewable energy sources in a cost-effective manner.

**Keywords:** doubly fed induction generators; fault detection; low-voltage ride-through; microgrids; wind farms



**Citation:** Kandil, T. Investigation of the Impact of Fault Characteristics on the Cost-Effectiveness of Doubly Fed Induction Generator-Based Wind Systems in Withstanding Low-Voltage Ride-Through. *Sustainability* **2024**, *16*, 5812. <https://doi.org/10.3390/su16135812>

Academic Editor: Mohamed A. Mohamed

Received: 7 June 2024

Revised: 28 June 2024

Accepted: 3 July 2024

Published: 8 July 2024



**Copyright:** © 2024 by the author. Licensee MDPI, Basel, Switzerland. This article is an open access article distributed under the terms and conditions of the Creative Commons Attribution (CC BY) license (<https://creativecommons.org/licenses/by/4.0/>).

## 1. Introduction

The largest energy company in North Carolina (NC), Duke Energy, recently released a report indicating that numerous significant changes to the energy landscape will have an impact on its future expansion plan over the next ten years [1,2]. These include the following:

- An anticipated large increase in demand and reserve capacity;
- Cleaner energy sources than coal power plants have to be used due to the policy of regulatory environment;
- The incentives offered by the Inflation Reduction Act (IRA) of 2022 and the Infrastructure Investment and Jobs Act (IIJA) for customers to use solar energy and electric vehicles, which require more energy to be generated and follow a different load curve behavior than the traditional ones;
- The challenges posed by the risen inflation and supply chain issues;
- The technological innovations and consumer preferences that shape resource choices and timing.

It is worth mentioning that approximately 85 GW of the USA's coal-fired plants were retired between 2012 and 2021, and about 25% of the remaining plants are projected to retire by 2029 [3]. Further, NC is undergoing rapid expansion as they are attracting

not only residential consumers but also major industrial and commercial enterprises, which necessitate a more environmentally friendly generation mix for them to relocate or remain in NC. Therefore, the retiring coal capacity must be substituted with equally reliable resources to preserve or improve reliability before that baseload generation ceases operation [2]. Among these resources are renewable energy resources (RESs), which are mostly solar, wind, and hydro, which will help reduce the dependence on fossil fuels, lower the carbon footprint, and diversify the energy mix. Among the various renewable energy resources (RESs) that Duke Energy is planning to use extensively in the next 10 years is wind energy [3], which can also be integrated with other RESs, such as solar, hydro, and battery storage, to create hybrid systems that can provide reliable and flexible power [4–6]. Further, the concept of MGs, which supply electricity to nearby consumers and strengthen the reliability and safety of the power grid, was also introduced due to the growing usage of RESs and DGs. Power quality and efficiency can be optimized, transmission and distribution losses can be minimized, and MGs can keep the power on in the event of an emergency or grid outage [7–10]. However, MGs also pose some technical challenges, especially with respect to protection and coordination, as MGs need to have proper protection devices and schemes to prevent faults and damages and to coordinate with the main grid. However, MGs' protection and coordination are complicated due to the bidirectional power flows, variable generation, and different operating modes of MGs [7–10]. Moreover, the greater deployment of wind turbines and large distributed generators might result in elevated fault current levels, as well as reduced voltage levels at the terminals of wind turbines during a failure. The consequences of these impacts can result in the complete interruption of wind turbines, leading to grid instability. To address this issue, sophisticated protection methods, control circuits or external devices, such as, but not limited to, adaptive relays, smart circuit breakers, fault current limiters, and STATCOM, are necessary to be employed [11–13].

One of the most essential concepts in maintaining power system stability is the low-voltage ride-through (LVRT) capabilities during transitory system transients or failures. LVRT is the ability of electric generators, such as wind turbines and photovoltaic systems, to remain connected and stable during short periods of low voltage in the grid. LVRT is essential for preventing cascading failures and blackouts and supporting grid recovery [14–20]. For example, a code was presented, in [14], which keeps the DG connected if the system nominal voltage drop stays above 30% of nominal voltage drop ( $V_g$ ) for 0.5 s, and then recovers to at least 90% of  $V_g$  in 1.5 s or less, as shown in Figure 1. The DG could disconnect if the voltage drops below the proposed curve. Further, the voltage control circuit of the WT has to react within 20 ms from fault detection to provide enough reactive power to keep the grid voltage within the permissible limits [17]. Nevertheless, as shown in Figure 2, MGs that utilize wind generators are needed to adhere to the various operational constraints that various countries have put in place for LVRT [21,22]. This is due to various factors, including the extent of renewable energy penetration, local utility policies, and the unique technical requirements of respective power systems. Furthermore, the grid code for LVRT differs in each country, depending on the requirements of transmission system operators (TSOs). These operators are in charge of preserving the power system's stability, and they establish LVRT regulations to ensure that wind turbines and other renewable energy sources can tolerate voltage drops without disconnecting from the grid [23,24]. Further, different countries may have varying degrees of infrastructure strength, technology innovation, and regulatory frameworks, resulting in different LVRT requirements. For example, a country with a strong wind energy penetration may have stricter LVRT regulations to address the greater impact of voltage dips on its grid system. Furthermore, environmental factors such as lightning strike frequency and grid faults might have an impact on LVRT requirements. Countries with more frequent disturbances may need more resilient LVRT capabilities to keep the grid stable. In conclusion, the differences in LVRT codes between countries reflect their distinct electrical system characteristics, regulatory contexts, and the unique issues they confront when incorporating renewable energy sources into their networks.

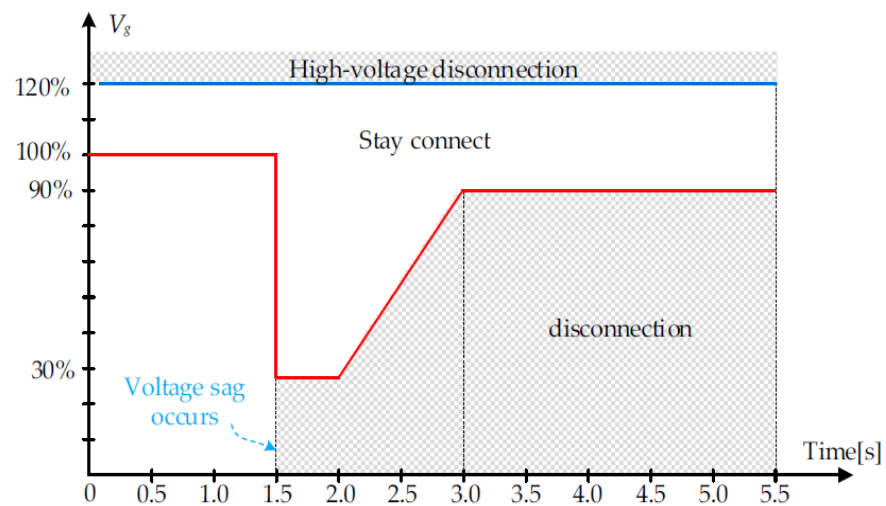


Figure 1. Requirements for low-voltage ride-through (LVRT) capability.

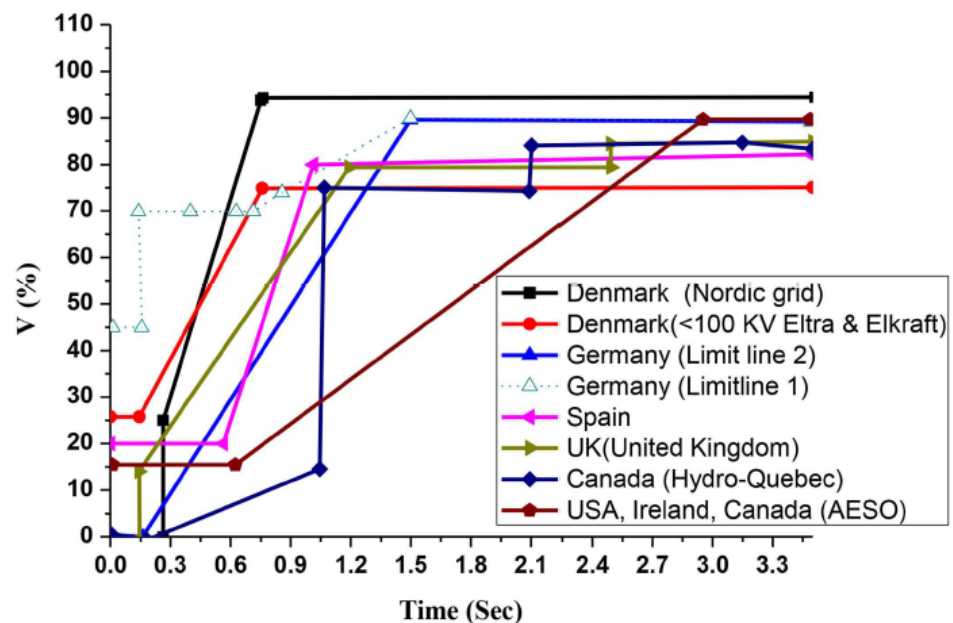


Figure 2. LVRT codes for different countries.

As a result, there is a significant need for research and focus into the effect of various fault types and characteristics on the detection of LVRT events to effectively select the appropriate code that assures system stability as this subject has not received sufficient research attention in the existing literature. Furthermore, the current study focuses on how the DFIG-WT, shown in Figure 3, responds to power system faults, as this type of generator is commonly used to generate electricity from wind energy.

Two voltage source converters—the rotor-side converter (RSC) and the grid-side converter (GSC)—connect the DFIG's rotor to the grid.

The electrical grid is directly connected to its stator of the DFIG. While the GSC controls the power delivered and the DC link voltage, the RSC optimizes the quantity of power output to the grid. DFIG is hence highly vulnerable to utility grid disturbances because the stator and GSC are directly connected to the grid bus voltage. Therefore, an excessive rotor overcurrent could develop from a loss of grid power, raising the DC link voltage and tripping the generator. As a result, numerous control and protection solutions have been proposed in the literature to maintain LVRT running in the event of a system fault [25–27], which include the following:

- Exterior LVRT techniques, including protection-based techniques, FACTS-based techniques, and hybrid approaches.
- Interior LVRT techniques, including tactics based on control strategies.

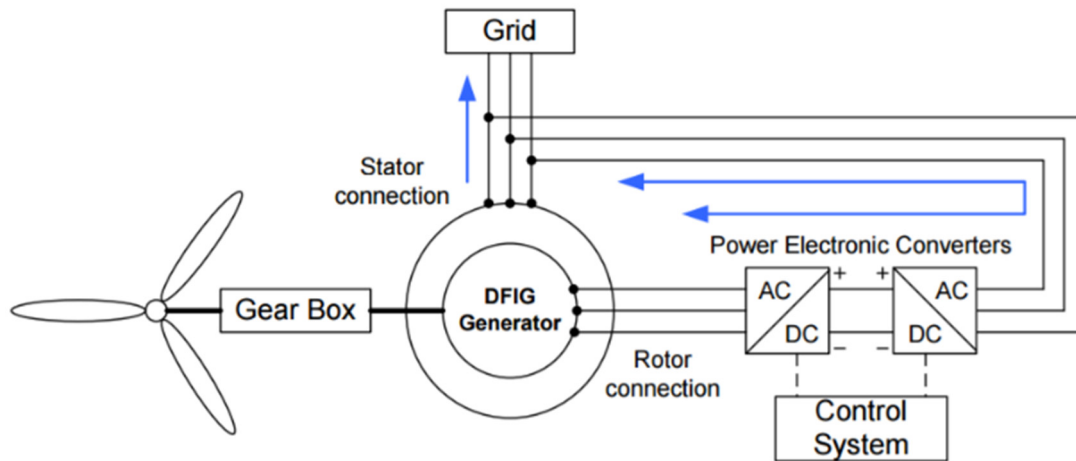


**Figure 3.** Doubly fed induction generator-based wind turbine.

The utilization of interior LVRT techniques offers improved control capabilities without the need for supplementary external circuits. Consequently, they provide more economic benefits but are more complex to execute [17–29]. This classification encompasses several control techniques, such as hysteresis control, modified vector control, fuzzy and sliding mode control, and model predictive control [30,31].

Nevertheless, the LVRT capability of the DFIG is significantly influenced by the appropriate calibration of the controller to adjust for sudden changes. The LVRT can be improved by modifying the control of the DFIG converter, which involves adjusting the control reference values. Conversely, external LVRT approaches are frequently employed because of their straightforwardness. Nevertheless, the financial aspect continues to pose a substantial barrier to the extensive use of these technologies. This classification encompasses utilizing crowbar in the rotor windings which is a prevalent method to decrease rotor currents and protect the DFIG from disturbances [32–34]. However, it is incapable of supplying the necessary reactive power to meet the grid's demands [35,36]. A chopper-based approach to control the DFIG DC-link was suggested to address the crowbar problems [37,38], but it resulted in excessive current in the RSC during faults. Shunt capacitors and STATCOMs are classified within this category; however, they lack efficacy in mitigating unsymmetrical faults [21,39]. In [40,41], a DVR-based LVRT technique was suggested; however, it exhibits significant control complexity and computational requirements. Ultimately, the choice of LVRT techniques for wind turbines is determined by the equilibrium between simplicity, cost, and effectiveness.

Hence, in order to choose, develop, and execute appropriate LVRT methods for wind turbines, such as external devices, advanced controllers, or hybrid approaches, it is imperative to understand the impact of fault characteristics on the wind energy system during a fault. These characteristics include fault resistance, type, location, duration, and severity, all of which influence the voltage and frequency profiles of the grid, as the ground fault currents may be reduced substantially when fault resistance is included in the fault circuit. Most faults that occur on a power system involve the ground and occur between the conductor and tower. When a fault occurs to a steel tower or grounded wood pole on a grounded system, the footing resistance is included automatically in the fault circuit and the resulting ground current may be materially less than that calculated when neglecting the fault resistance.

Therefore, the primary objective of this study is to perform a qualitative analysis of the impact of fault characteristics on the system's performance during voltage dips, as this

subject has not been extensively studied in the literature. The efficacy of a power system model is evaluated through the examination of various fault types and scenarios. The analysis has the potential to offer valuable insights and recommendations for enhancing the LVRT of the power system in a cost-effective manner.

The subsequent sections of the article are structured in the following manner: Section 2 presents a concise summary of the power system employed in the research. Section 3 presents an analysis of the dynamic behavior of both the stator and rotor of the DFIG during a grid fault. Section 4 discusses the influence of different fault characteristics on DFIG during LVRT events, offers suggestions for selecting LVRT methods or approaches, gives case studies, and presents the findings of the system evaluation. This paper is concluded in Section 5 which also provides suggestions for future directions.

## 2. Overview of the Power System Utilized in the Research

Figure 4 depicts a diagram of the power system employed in this investigation. The grid has a 25 kV, 60 Hz generating station. It is connected to the MG via a 132 kV transmission line. Furthermore, the MG has a local 20 MVA wind farm (WF) that transmits its power through a 0.575/13.8 kV step-up transformer. Three 10 MVA loads are positioned at 13.8 kV and supplied by both the WF and the utility generator. The loads being studied are described as follows:

Load-1 is a linear inductive load with 0.75 power factor.

Load-2 is a non-linear load (3-phase rectifier bridge with RL load) that has 15% THD.

Load-3 is an induction motor.

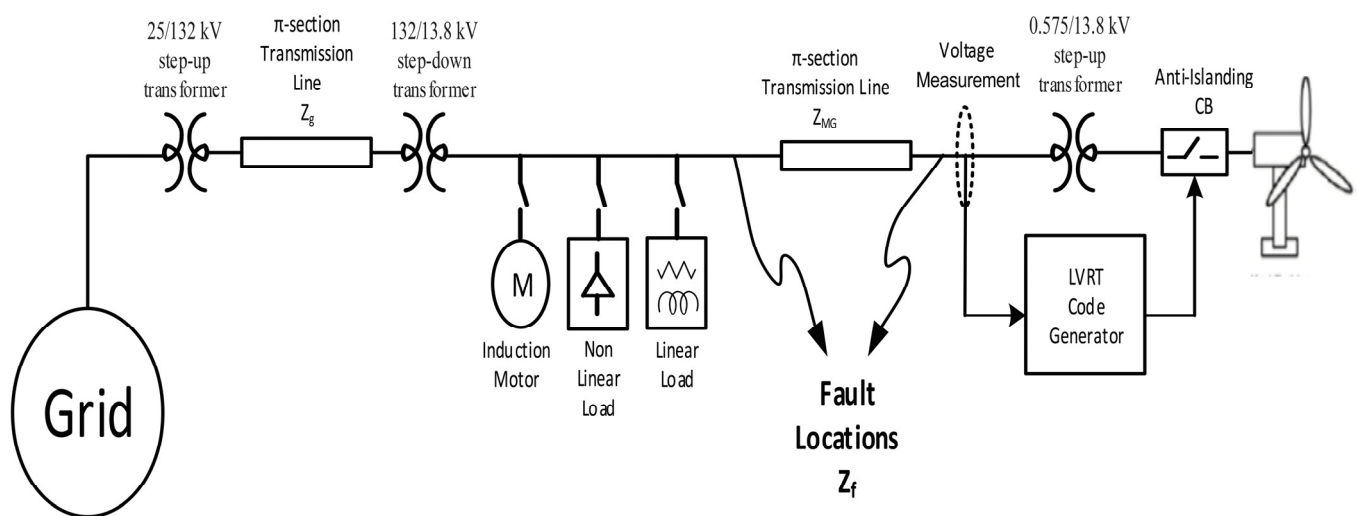
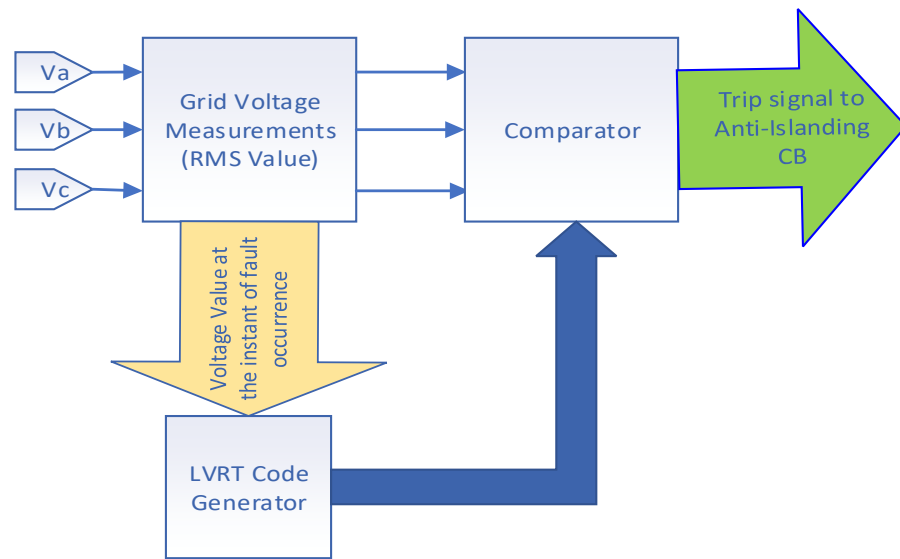


Figure 4. Single-line diagram of the system under study.

The block diagram for generating the tripping signal of the LVRT circuit breaker is shown in Figure 5. The tripping signal for the anti-islanding circuit breaker is created using the following procedure:

1. The rms value of the pre-fault voltage,  $V_{pre-fault}$ , is measured and locked during the fault time.
2. The LVRT code is generated using the  $V_{pre-fault}$ .
3. Finally,  $V_{pre-fault}$  is compared with the LVRT code and processed through the logic circuit to generate the tripping signal for the circuit breaker.

It is important to note that the time frame for measuring the rms value of  $V_{pre-fault}$  should be kept as short as possible to avoid causing delays or interruptions in the operation of the LVRT code generator. However, it should still be sufficient to accurately capture the voltage value.



**Figure 5.** Block diagram of the LVRT control circuit to generate CB trip signal.

### 3. Introduction to Dynamic Behavior of DFIG under Grid Fault

#### 3.1. Dynamic Behavior of DFIG Stator

Regions with ample wind energy are typically located at a considerable distance from power hubs. Consequently, the establishment of large WFs facilitates the transmission of wind power to the power system across considerable distances. The transformer that connects the DFIG to the grid often has a  $\Delta/Y$  connection. Consequently, when faults occur, it is necessary to simply evaluate the positive- and negative-sequence components of the DFIG. In normal operation, the stator voltage space phasor is a rotating vector of constant amplitude,  $V_s$ , that rotates at synchronous speed  $\omega_s$ :

$$\vec{v}_s = V_s e^{j(\omega_s t)} \quad (1)$$

The expression for the post-fault stator voltage of the DFIG after accounting for transmission losses is as follows [42,43]:

$$\vec{v}_{s_{post-fault}} = \vec{v}_{s1} + \vec{v}_{s2} = (1-A)V_{pre-fault} e^{j(\omega_s t + \theta^+)} + V_{post-fault} e^{j(-\omega_s t + \theta^-)} \quad (2)$$

where  $\vec{v}_{s1}$  and  $\vec{v}_{s2}$  are the positive- and negative-sequence voltages,  $A$  is the sag ratio in the stator voltage.  $V_{pre-fault}$  is the amplitude of the pre-fault stator voltage;  $V_{post-fault}$  is the amplitude of the post-fault stator voltage; and  $\theta^+$  and  $\theta^-$  are the phase angles of  $\vec{v}_{s1}$  and  $\vec{v}_{s2}$  at the starting of the fault, e.g., time  $t = 0$ .

Although the representation and symbols of the DFIG-equivalent circuits differ depending on the regions, they all share the same principle and provide equal results. Therefore, the stator positive- and negative-sequence short circuit currents can be determined using those circuits shown in Figure 6, within a synchronous rotating reference frame [42–44].

$$\begin{aligned} \vec{i}_{s1} &= -\frac{AV_{pre-fault}}{j\omega_s L'_s} e^{(\frac{-t}{T'_s} + j\theta^+)} + \frac{L_m}{L'_s L_r} \left[ \vec{\varphi}_{r0} - f_1(s) \frac{(1-A)V_{pre-fault}}{j\omega_s} e^{j\theta^+} \right] e^{\frac{-t}{T'_r} + j\omega_r t} \\ &\quad + \left[ \frac{L_m}{L_r} f_1(s) - 1 \right] \frac{(1-A)V_{pre-fault}}{j\omega_s L'_s} e^{j(\omega_s t + j\theta^+)} \\ \vec{i}_{s2} &= -\frac{V_{post-fault}}{j\omega_s L'_s} e^{(\frac{-t}{T'_s} + j\theta^-)} + f_2(s) \frac{L_m}{L'_s L_r} \times \frac{V_{post-fault}}{j\omega_s} e^{\frac{-t}{T'_r} + j(\omega_r t + \theta^-)} \\ &\quad - \left[ \frac{L_m}{L_r} f_2(s) - 1 \right] \frac{V_{post-fault}}{j\omega_s L'_s} e^{j(-\omega_s t + j\theta^-)} \end{aligned} \quad (3)$$

where

$\omega_s =$  Synchronous frequency,  $\omega_r =$  Rotor frequency

$$L'_s = L_s - \frac{L_m^2}{L_r}, L'_r = L_r - \frac{L_m^2}{L_s}, f_1(s) = \frac{\frac{R_r L_m}{L_s}}{R_r + j(\omega_s + \omega_r)L'_r}, f_2(s) = \frac{\frac{R_r L_m}{L_s}}{R_r - j(2-s)\omega_s L'_r}$$

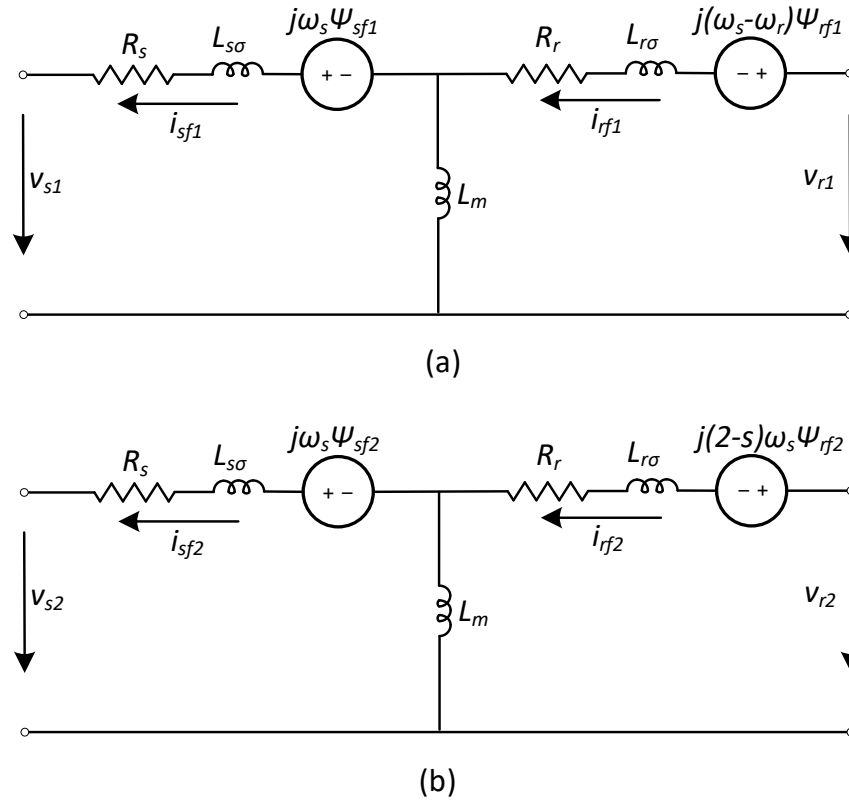


**Figure 6.** The synchronous rotating reference frame equivalent circuits of DFIG: (a) the positive-sequence-equivalent circuit and (b) the negative-sequence-equivalent circuit.

$$T'_s = \frac{L'_s}{R_s}, T'_r = \frac{L'_r}{R_r}, s = slip = \frac{\omega_r}{\omega_s}, \vec{\varphi}_{r0} = \text{The pre-fault rotor flux linkage.}$$

When examining the actual values of the wind-based DFIG [43], it is observed that the stator and rotor resistances are significantly smaller than the stator, rotor, and mutual inductances. Consequently, it is reasonable to assume that the values of  $f_1(s)$  and  $f_2(s)$  are insignificant. Therefore, the currents in Equation (3) can be simplified as follows:

$$\begin{aligned} \vec{i}_{s1} &= -\frac{AV_{pre-fault}}{j\omega_s L'_s} e^{(\frac{-t}{T'_s} + j\theta^+)} + \frac{L_m}{L'_s L_r} \vec{\varphi}_{r0} e^{\frac{-t}{T'_r} + j\omega_r t} - \frac{(1-A)V_{pre-fault}}{j\omega_s L'_s} e^{j(\omega_s t + j\theta^+)} \\ \vec{i}_{s2} &= -\frac{V_{post-fault}}{j\omega_s L'_s} e^{(\frac{-t}{T'_s} + j\theta^-)} + \frac{V_{post-fault}}{j\omega_s L'_s} e^{j(-\omega_s t + j\theta^-)} \end{aligned} \quad (4)$$

As can be revealed by Equation (4), the stator short circuit current consists of three components: a decaying direct current (DC) component, a decaying AC component at the rotor speed frequency, and a forced AC component at the synchronous frequency. Typically, the magnitude of the forced AC component is negligible, especially in cases where the voltage drop is substantial, which signifies a considerable value of A. The decaying DC and AC components are the principal components of the short circuit current in such circumstances. The assessment of defect attributes in a transmission line-connected DFIG-WF is accomplished through the examination of the DFIG's short circuit current.

### 3.2. Dynamic Behavior of DFIG Rotor

Under normal conditions, and considering the DFIG's equivalent circuit shown in Figure 7, the voltage required to be produced by the converter at the rotor terminals can be mathematically represented as [45]:

$$\vec{v}_r = \frac{L_m}{L_s} \left( \frac{d}{dt} - j\omega \right) \vec{\varphi}_s + \left[ R_r + L'_r \left( \frac{d}{dt} - j\omega \right) \right] \vec{i}_r \quad (5)$$

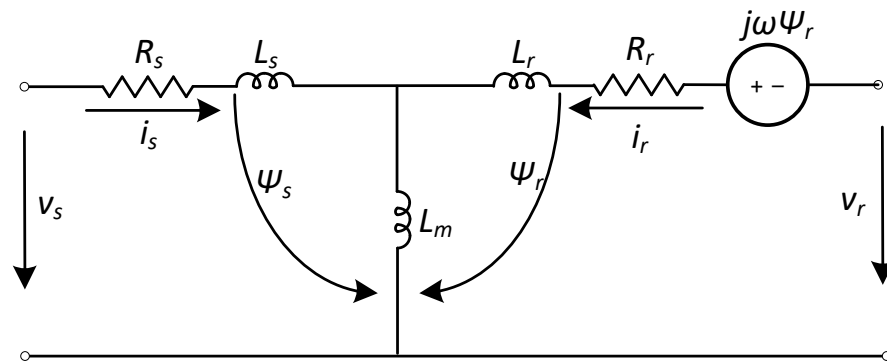


Figure 7. DFIG equivalent circuit.

If the stator resistance is neglected, Equation (5) can be simplified as

$$\vec{v}_r = \vec{v}_s \frac{L_m}{L_s} s + \left[ R_r + L'_r \left( \frac{d}{dt} - j\omega \right) \right] \vec{i}_r \quad (6)$$

where  $\omega = \text{slip frequency} = \omega_s - \omega_r$ .

The rotor resistance and the transient inductance are often very small. In addition, rotor currents also have a small frequency ( $\omega_r < 10$  Hz). Consequently, the voltage at rotor terminals can be expressed as

$$\begin{aligned} \vec{v}_r &= \vec{v}_s \frac{L_m}{L_s} s \\ V_r &= V_s \frac{L_m}{L_s} s \end{aligned} \quad (7)$$

However, during fault condition, the evolution of the stator flux obtained from (1) at  $t_0 = 0$  is as follows:

$$\begin{aligned} \vec{\varphi}_s (t < t_0) &= \vec{\varphi}_{s \text{ forced}} = \frac{V_s}{j\omega_s} e^{j(\omega_s t)} \\ \vec{\varphi}_s (t \geq t_0) &= \vec{\varphi}_{s \text{ forced}} = 0 \\ \vec{\varphi}_s (t \geq t_0) &= \vec{\varphi}_{s \text{ natural}} = \vec{\varphi}_0 e^{(-\frac{t}{\tau_s})} \end{aligned} \quad (8)$$

where  $\vec{\varphi}_0$  = stator flux just before the voltage dip.

Using Equations (8) and (5) and neglecting the term  $(1/\tau_s)$  due to its low value, this rotor voltage amplitude can be obtained as

$$V_r = V_s \frac{L_m}{L_s} (1 - s) \quad (9)$$

where  $V_r$  is proportional to  $(1 - s)$  as seen from Equation (9). Conversely, during regular operation, the steady-state rotor voltage exhibits a direct proportionality to  $(s)$ , as denoted by Equation (7). The slip is typically limited to a range of  $-0.2$  to  $0.2$  [44]. Therefore, it can be inferred that the magnitude of the voltage generated in the rotor during the initial dip is comparable to the rated voltage of the stator, rather than the small proportion generated during regular operation. Thus, during a single-line-to-ground (SLG) fault at phase (a) at the fifth second for a duration of 150 ms, as shown in Figure 8, there is a significant increase in the rotor current, regularly from 3 to 4 times the steady-state current, leading to increased mechanical loads on the rotor and other related components. Further, the

objective of the rotor-side converter (RSC) is to ensure that the stator voltage remains at the frequency of the grid. However, the stator voltage deviates in both magnitude and phase from the grid voltage due to the malfunction, as illustrated in Figure 9. Specifically, there is a phase shift of approximately 25 degrees. Consequently, the rotor voltage also varies, which impacts the functioning of the DFIG.

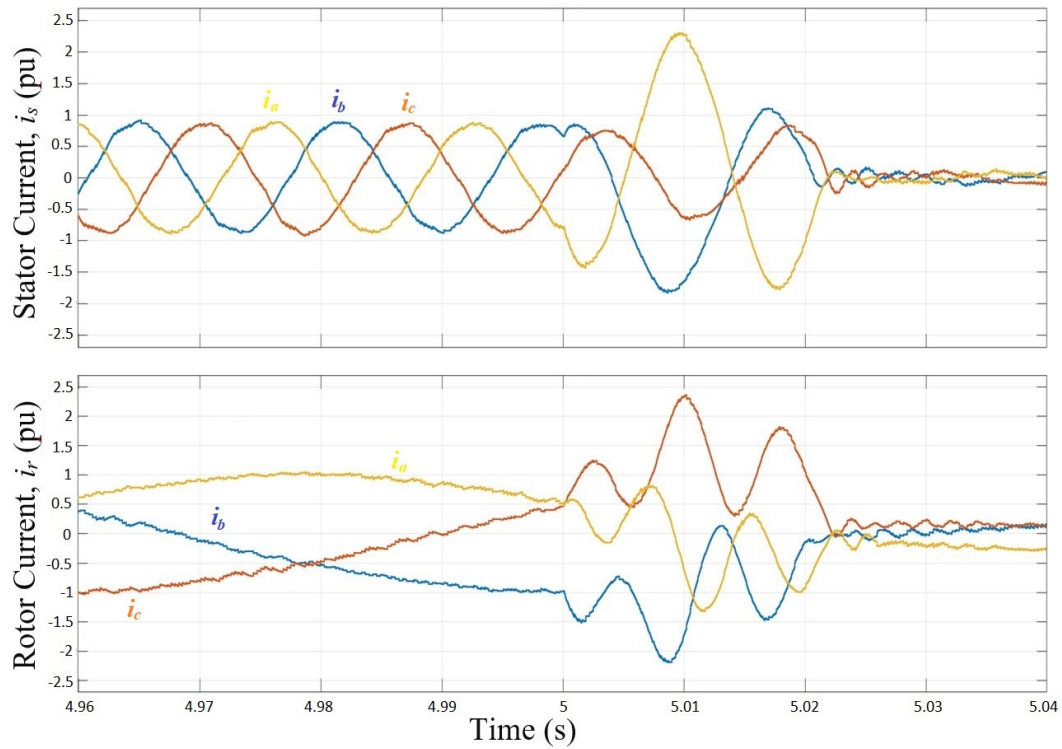


Figure 8. Stator current,  $i_s$ , and rotor current,  $i_r$ , during SLG fault at phase (a) at the 5th second.

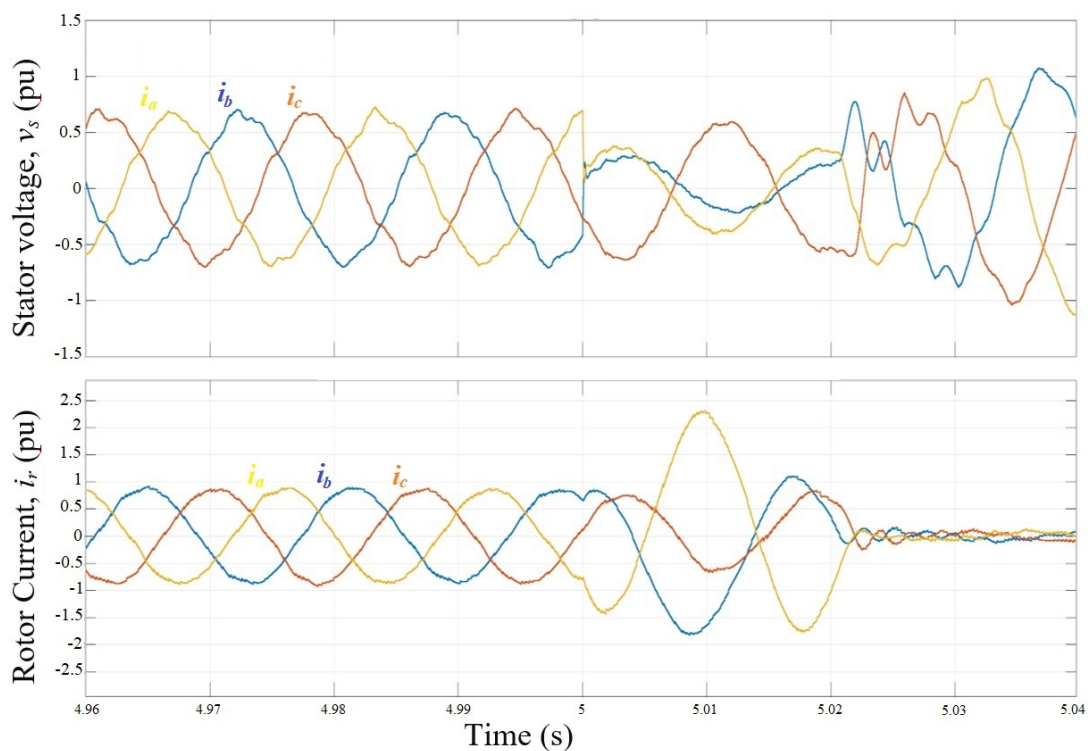


Figure 9. Stator voltage,  $v_s$ , and stator current,  $i_s$ , during SLG fault at phase (a) at the 5th second.

#### 4. Response of DFIG to Fault Characteristics

The impact of fault resistance on LVRT varies depending on the type of fault and the specific LVRT technology employed. Due to the possibility of several types of failures in the power system, such as grid disturbances, voltage sags, and short circuits, the fault resistance plays a crucial role in determining the speed at which faults are detected and their impact on system stability. For example, a high level of fault resistance can lead to a less significant decrease in voltage during a fault. In this situation, the DFIG can continue supplying reactive power to enhance grid support, allowing for the utilization of the crowbar approach by using a resistor to shorten the rotor terminals during an overvoltage and directing extra current away from the RSC, despite its consumption of reactive power from the grid. Conversely, a reduction in fault resistance results in more significant voltage dips, requiring the DFIG to respond quickly to maintain stability and supply reactive power for prompt voltage restoration. Hence, the utilization of the crowbar strategy may not be suitable in this specific scenario or may require the addition of another technique to ensure the ability to endure LVRT. Therefore, the efficiency of the LVRT methods employed relies heavily on the specific characteristics and the resistance of the fault. Three criteria can be used to categorize fault resistance,  $Z_F$ :

- Bolted fault,  $Z_F = 0$ ;
- Arcing fault,  $Z_F = \text{arcing resistance}$ ;
- Transmission-line insulator flashover,  $Z_F = \text{arc resistance} + \text{transmission tower resistance} + \text{the tower footing resistance}$ .

It should be emphasized that fault resistance is also affected by various factors, including but not limited to, the duration of the fault as longer fault durations can cause changes in resistance due to heating and material behavior. Other factors include ambient temperature and pressure, as well as the characteristics of the faulted conductor, such as its material, diameter, and surface condition. Therefore, engineers must consider fault characteristics and LVRT technique to ensure reliable grid integration of renewable energy sources.

When the fault resistance is present in the fault circuit, as shown in Figure 10, the fault current drawn from the WF,  $i_{wf}$ , can be calculated as follows.

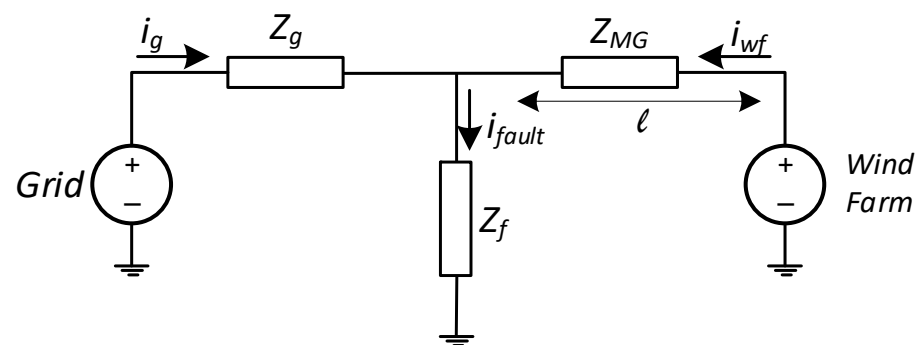


Figure 10. Simplified model of power system during fault.

$$\begin{aligned}
 \vec{i}_{fault} &= \vec{i}_{wf} + \vec{i}_g \\
 \vec{v}_{wf} &= \vec{v}_{MG} + \vec{v}_{fault} \\
 \vec{v}_{wf} &= Z_{MG} \vec{i}_{wf} + Z_f (\vec{i}_{wf} + \vec{i}_g) \\
 \vec{i}_{wf} &= \frac{\vec{v}_{wf} - Z_f \vec{i}_g}{Z_{MG} + Z_f}
 \end{aligned} \tag{10}$$

It can be concluded from Equation (10) that the short circuit currents may be significantly decreased with the increase in fault resistance. However, since the footing resistances of each tower connected to the ground wire are parallel, the effective fault resistance is

significantly decreased when the transmission-line towers are tied together with overhead ground wires next to the substation.

Therefore, to ensure an adequate footing resistance value in the fault circuit, the ground wire must be insulated from both the towers and the station ground mat. This means that only one tower per circuit is recommended to be connected to the ground wire to dissipate static charge.

#### 4.1. Response of the DFIG to Single-Line-to-Ground Fault

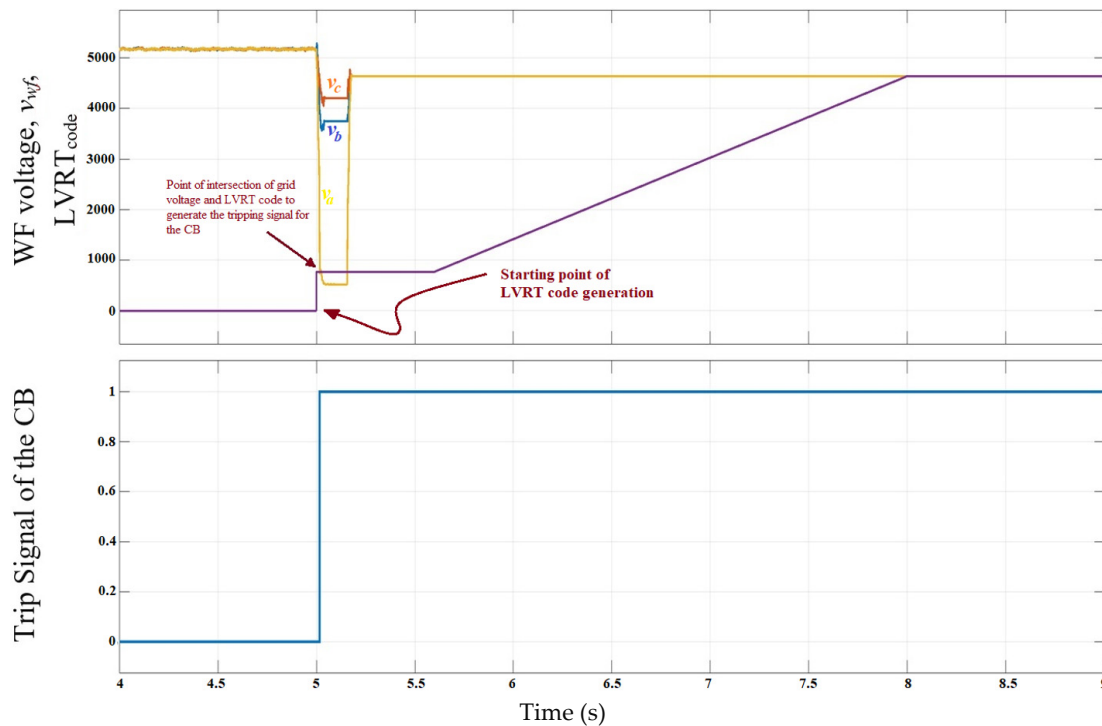
Given that SLG faults account for about 70–80% of all faults in the power system [46–48], it is critical to begin to understand how DFIG responds to these faults. At the fifth second of the simulation, a single-phase bolted fault incident,  $Z_F = 0$ , occurs for 150 ms on the high voltage side of the WF's transformer, i.e., more precisely, between phase (a) and the ground. This indicates that the length of the line is  $l = 0$ , and hence,  $Z_{mg} \approx 0$ . As a result, the positive, negative, and zero sequences of the WF's fault currents are all equal and may be calculated as follows using the symmetrical component concept:

$$\left| \vec{i}_{wf1} \right| = \left| \vec{i}_{wf2} \right| = \left| \vec{i}_{wfo} \right| = \frac{\left| \vec{v}_{wf} - Z_f \vec{i}_g \right|_{pre-fault}}{Z_{mg1} + Z_{mg2} + Z_{mgo} + 3Z_f} \quad (11)$$

Further, the current drawn from phase (a) of the WF can be determined as

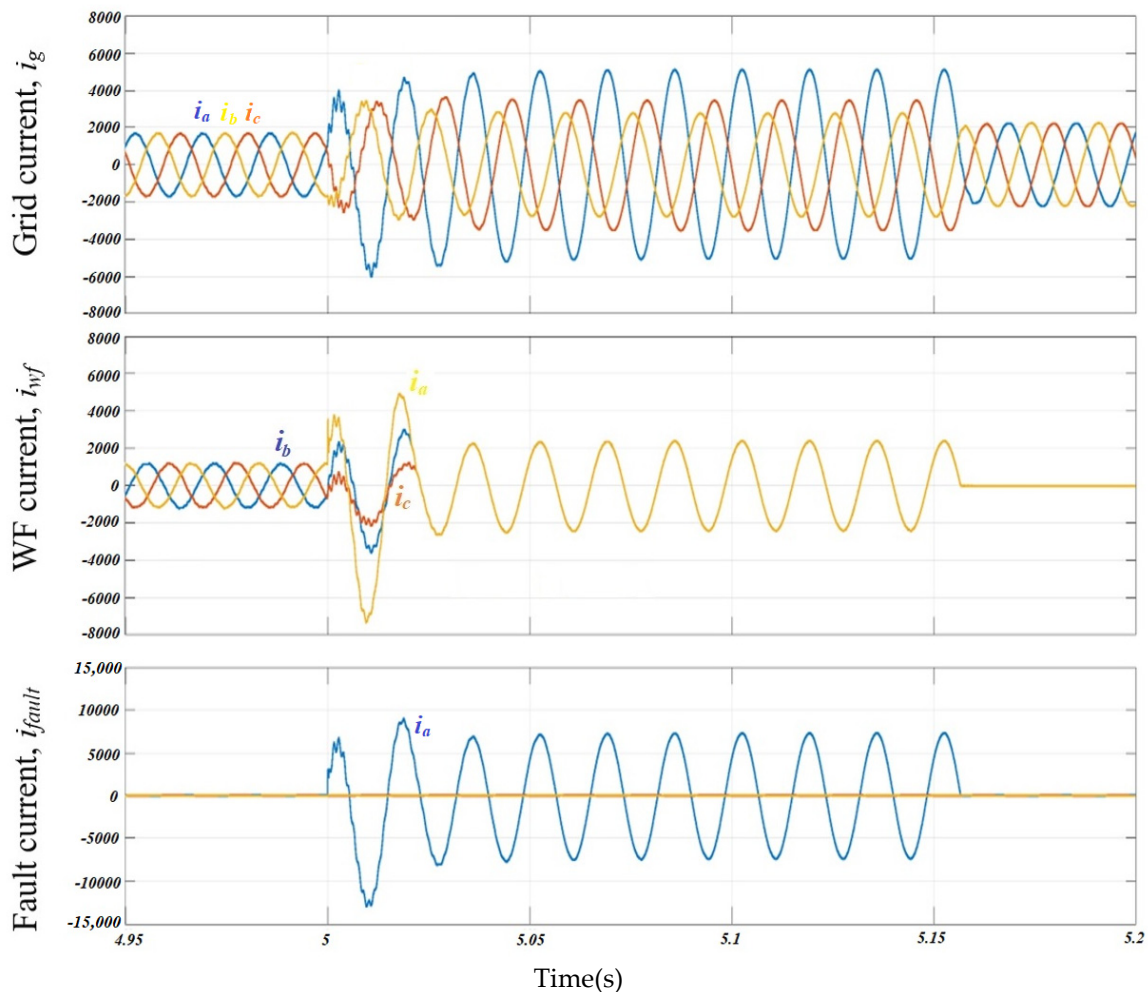
$$\left| \vec{i}_{wfa} \right| = \left| \vec{i}_{wf1} \right| + \left| \vec{i}_{wf2} \right| + \left| \vec{i}_{wfo} \right| = \frac{3 \left| \vec{v}_{wf} - Z_f \vec{i}_g \right|_{pre-fault}}{3Z_f} = \frac{\left| \vec{v}_{wf} - Z_f \vec{i}_g \right|_{pre-fault}}{Z_f} \quad (12)$$

Figure 11 depicts the response of the three-phase RMS voltages of the WF and LVRT code generated, demonstrating that due to the very low fault resistance and close proximity to the WF, the fault at phase (a) was strong enough to violate the LVRT's safety measure, causing the anti-islanding circuit breaker to trip and shut down and isolate the WF.



**Figure 11.** WF voltage,  $v_{wf}$ ,  $LVRT_{code}$ , and trip signal of the CB during SLG bolted fault ( $Z_F = 0$ ) at phase (a) at the 5th second.

By analyzing Figures 12 and 13, it is evident that the phase (a) current,  $i_{wfa}$ , experiences a sudden very high rise of about six times the rated value prior to the circuit breaker being triggered. Subsequently, the current persists in flowing towards the transformer's grounding system until the fault is cleared. The remaining phases similarly react to this fault by amplifying their currents until the fault is cleared. Consequently, the stator currents will be directly affected by these modifications. Further, as a result of the magnetic coupling that exists between the stator and rotor windings, the rotor currents are also perturbed in the same direction as the stator currents and an increase in current will be observed in both the stator and rotor windings, as previously shown in Figure 8.



**Figure 12.** Grid current,  $i_g$ , WF current,  $i_{wf}$ , and fault current,  $i_{fault}$ , during SLG bolted fault ( $Z_F = 0$ ) at phase (a) at 5th second.

However, if there is a considerable impedance in the fault,  $Z_F \gg 0$ , caused by factors such as arcing resistance, transmission tower resistance, or tower footing resistance,  $Z_F$  is only  $1 \Omega$  in this case, and the short circuit currents will be greatly reduced to only three times the rated current, as shown in Figure 14. As a result, the fault voltage, according to Equation (10), will experience a minor decrease in its value and consequently will meet the requirements of the LVRT code. Therefore, the anti-islanding circuit breaker will not trip, as depicted in Figure 15, allowing the WF to remain connected to the grid and preserve its stability. However, in the case of a prolonged fault duration, such as when the fault persists for several seconds, the phase voltage will fall below the 90% threshold required for LVRT and thus results in tripping the CB.

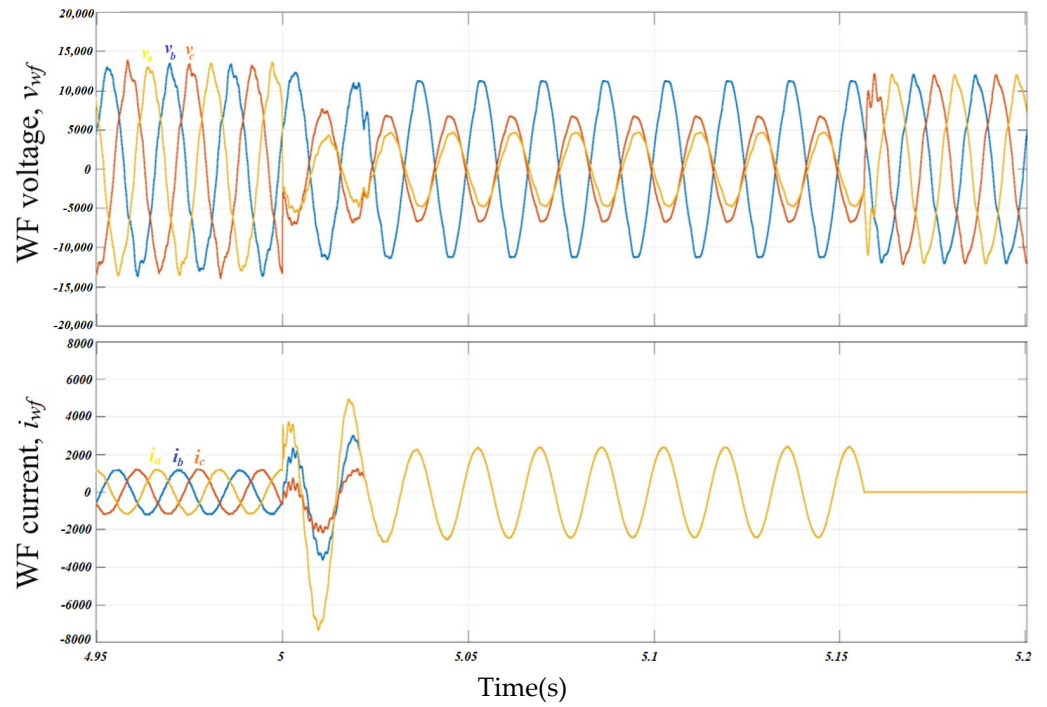


Figure 13. WF voltage,  $v_{wf}$ , and WF current,  $i_{wf}$  during SLG bolted fault ( $Z_F = 0$ ) at phase (a) at 5th second.

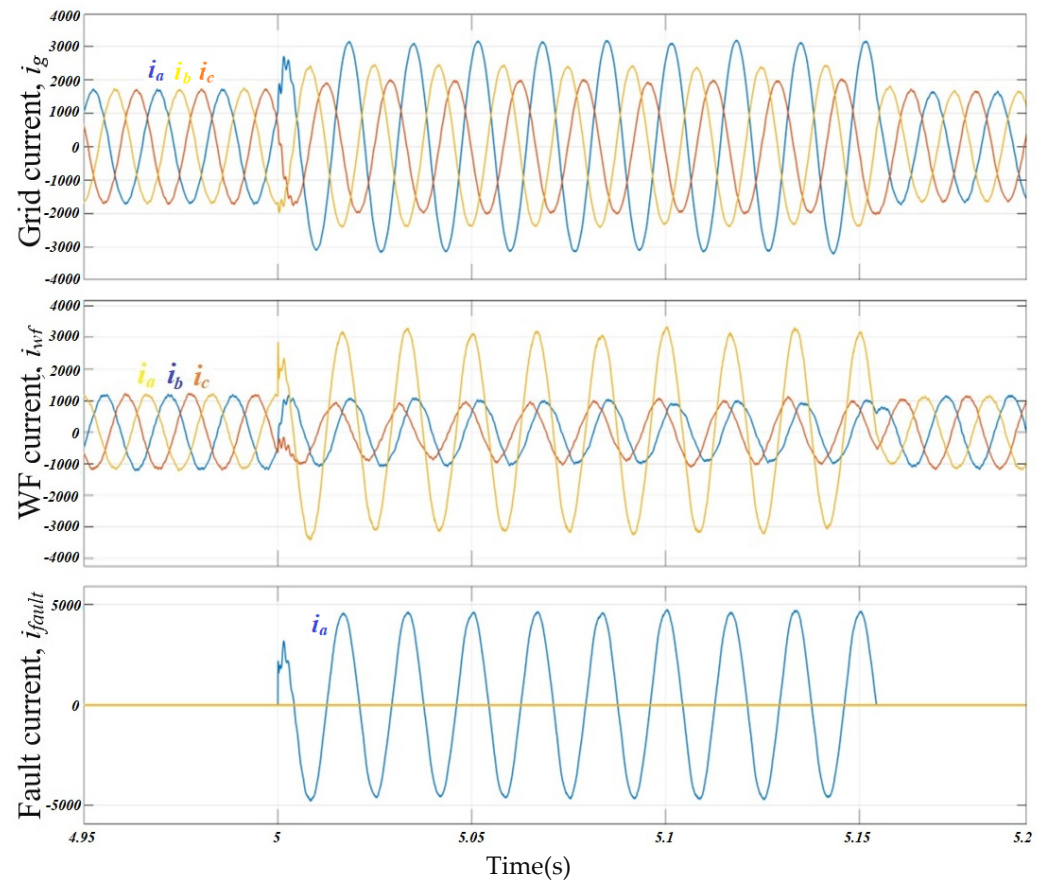
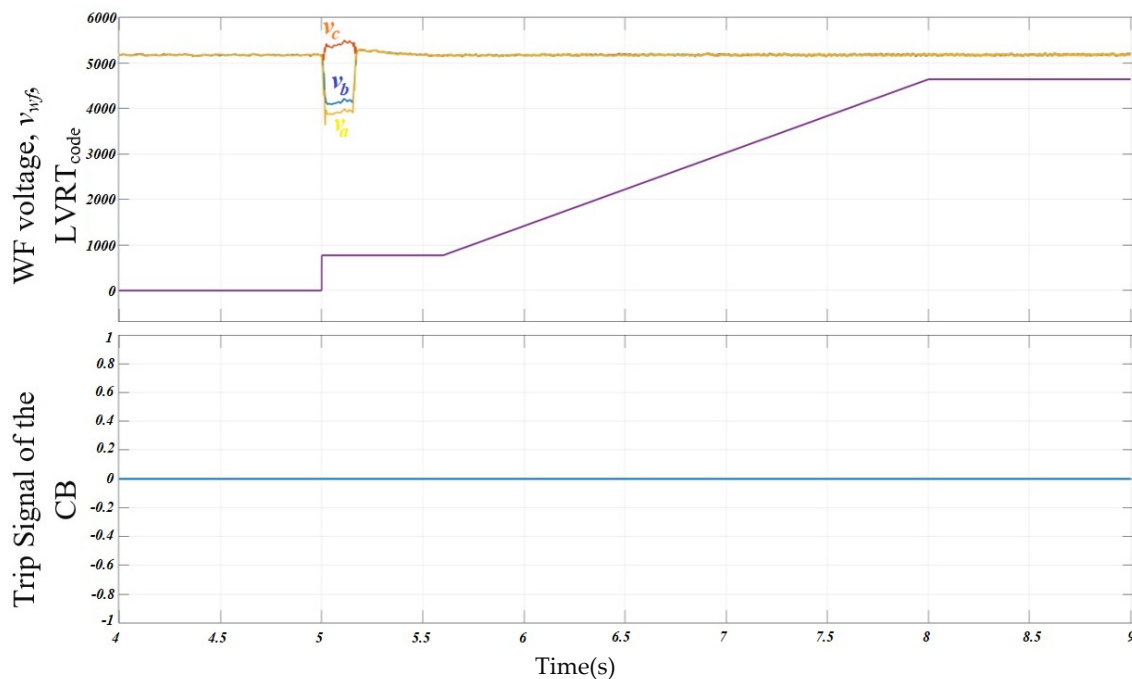


Figure 14. Grid current,  $i_g$ , WF current,  $i_{wf}$ , and fault current,  $i_{fault}$ , during SLG bolted fault at phase (a) when considering the arcing resistance, transmission tower resistance, or tower footing resistance ( $Z_F \gg 0$ ).



**Figure 15.** WF voltage,  $v_{wf}$ , LVRT<sub>code</sub>, and trip signal of the CB during SLG fault at phase (a) when considering the arcing resistance, transmission tower resistance, or tower footing resistance ( $Z_F \gg 0$ ).

Thus, to maintain a satisfactory level of resistance in the fault circuit, it is recommended to insulate the ground wire from both the towers and the station's ground mat. This is conducted to prevent a substantial decrease in fault resistance caused by the parallel connection of the transmission-line ground wires and to connect only one tower per circuit to the ground wire to dissipate static charges. Further, determining the appropriate LVRT code for a particular area is also highly dependent on the fault characteristics of that region.

Additionally, a comparable effect to the fault resistance will depend on the fault location. According to Equation (10), the farther the fault is from the WF, the larger the transmission-line impedance,  $Z_{MG}$ , and consequently, the lower the fault current that is pulled from the WF. Figure 16 shows the response of the WF for a single phase to ground voltage at 5 km from the WF, which reveals that a decrease in  $v_{wf}$  that will comply with the LVRT code and hence the anti-islanding circuit breaker will not trip, thereby allowing the WF to remain connected to the grid. Therefore, it is crucial to consider the impedance of the MG transmission line or cable while deciding on the suitable equipment or method to enhance the LVRT.

For example, one way to increase  $Z_{MG}$  during a fault is by utilizing superconducting fault current limiters (SFCLs), which offer zero resistance to currents up to a certain threshold value, and once the critical current is surpassed, the resistance of the superconductor rises, resulting in a decrease in the fault current. Nevertheless, this technology has several drawbacks, such as a substantial high price and the need for costly cooling components. In addition, the activation of SFCLs can lead to voltage drops, which can cause a decrease in voltage levels and impact the flicker factor at the point of common coupling. This is due to the rapid fluctuations in power from renewable energy sources. Thus, it is essential to incorporate the fault characteristics, e.g., in this case, in the design or selection of the protection device to enhance cost-effectiveness.

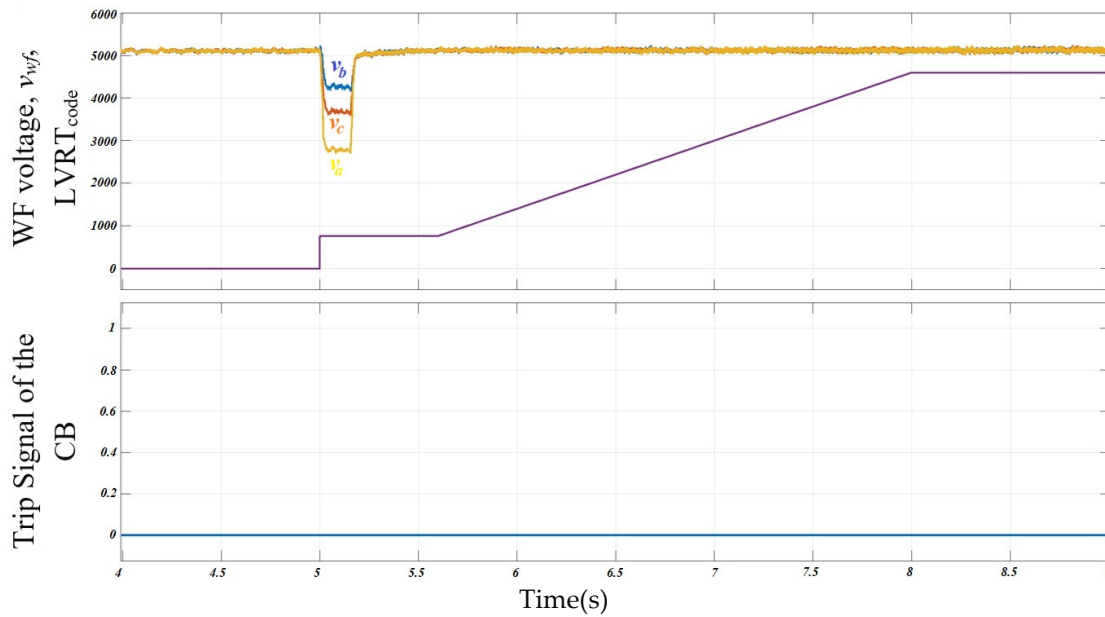


**Figure 16.** WF voltage,  $v_{wf}$ , LVRT<sub>code</sub>, and trip signal of the CB during SLG fault at phase (a) at 5 km distance from the WF.

#### 4.2. Response of the DFIG to Three-Phase-to-Ground Fault

Given that the three-phase-to-ground fault is the worst-case scenario in power systems but fortunately account for about 5–10% of all faults in the power system, it is important to investigate the response of the DFIG to these faults. At the fifth second of the simulation, a three-phase bolted fault incident,  $Z_F \approx 0$ , occurs for 150 ms on the high voltage side of the WF's transformer—more precisely, between phase (a) and the ground. This indicates that the length of the line is  $l = 0$ , and hence,  $Z_{mg} \approx 0$ .

During a bolted three-phase fault, the zero- and negative-sequence fault currents are  $I_0 = I_2 = 0$ , and as a result, the positive sequence of the WF's fault current may be calculated as follows using the symmetrical component concept:

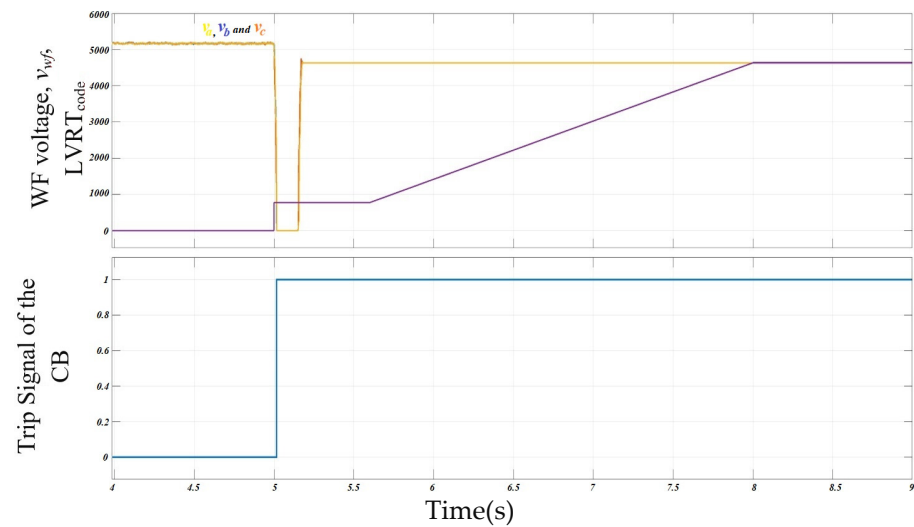
$$\left| \vec{i}_{wf1} \right| = \frac{\left| \vec{v}_{wf} - Z_f \vec{i}_g \right|_{pre-fault}}{Z_{mg1} + Z_f} \quad (13)$$

Finally, the currents drawn from the three phases of the WF can be determined as

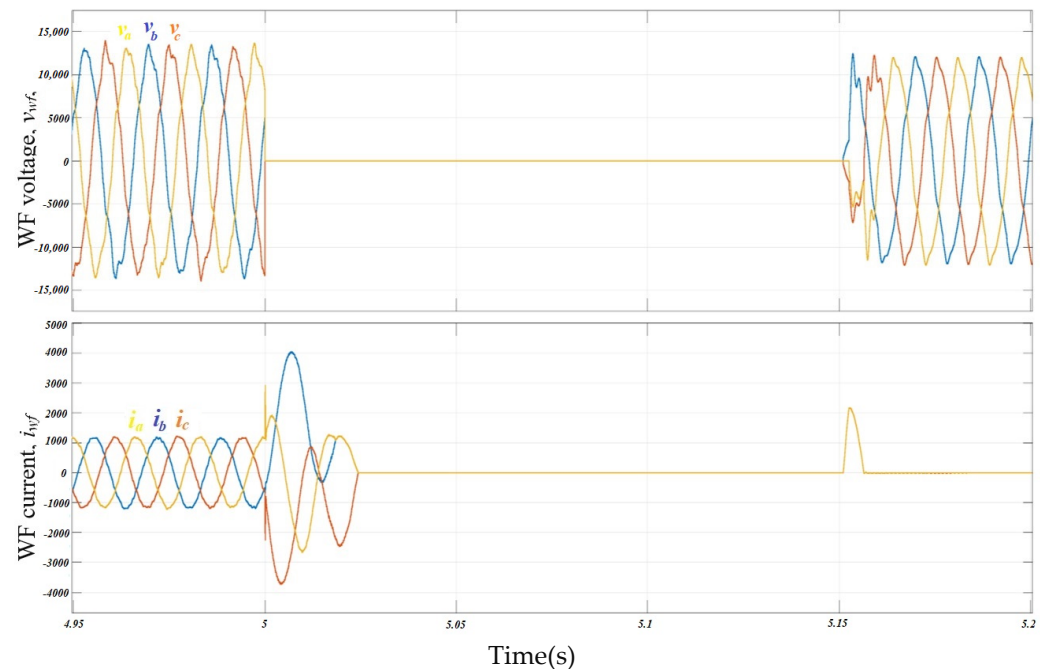
$$\left| \vec{i}_{wfa} \right| = \left| \vec{i}_{wfb} \right| = \left| \vec{i}_{wfc} \right| = \left| \vec{i}_{wf1} \right| = \frac{\left| \vec{v}_{wf} - Z_f \vec{i}_g \right|_{pre-fault}}{Z_f} \quad (14)$$

Figure 17 depicts the response of the three-phase RMS voltages of the WF and LVRT code generated, demonstrating that due to the very low fault resistance and close proximity to the WF, the fault at the three phases was strong enough to violate the LVRT's safety measure, causing the anti-islanding circuit breaker to trip and shut down and isolate the WF.

Figure 18 shows that the three-phase currents drawn from the WF rise to approximately three times the rated value before the circuit breaker is triggered. However, because the current has no zero-sequence component, it will cease to flow in the transformer's grounding system immediately after the CB trips. If the fault has a high impedance ( $Z_F \gg 0$ ), the voltage will decrease slightly, meeting the LVRT code criteria. As a result, the anti-islanding circuit breaker will not trip, allowing the WF to remain connected to the grid while maintaining its stability.



**Figure 17.** WF voltage,  $v_{wf}$ ,  $LVRT_{code}$ , and trip signal of the CB during three-phase ground bolted fault.



**Figure 18.** WF voltage,  $v_{wf}$ , and WF current,  $i_{wf}$  during three-phase ground bolted fault.

## 5. Conclusions

This paper investigates the impact of various fault characteristics on the LVRT capability of MGs to comply with grid codes during faults. The objective is to provide a clear picture for the grid response to different fault characteristics to help select the most suitable LVRT code and LVRT-enhancing technique, whether internal or external, and the appropriate ratings for these devices, with the aim of reducing the installation costs of WFs.

It is found that these characteristics significantly impact LVRT and the system stability, and in determining the speed at which faults are detected. For example, it is recommended to maintain adequate footing resistance and ground wire insulation from both towers and the station ground mat, which can greatly reduce short circuit currents and meet the requirements of the LVRT code. In addition, the total fault resistance and, accordingly, the fault currents, are influenced by various other factors such as fault location, fault duration, ambient temperature, pressure, and the properties of the faulty conductor. Therefore,

designers should consider all these factors to ensure the reliable integration of renewable energy sources into the grid at the lowest possible cost.

In addition, it is essential to consider the impedance of the transmission line between PCC and the WF when determining the appropriate LVRT code for a certain area. This impedance has a considerable effect on the impact of fault currents on the WF. It is highly desirable to increase the impedance during a failure to restrict the flow of fault currents. However, the devices employed for this purpose are quite expensive. Therefore, to lessen the financial burden on the system, it is crucial to employ an efficient design or lower the rating. The study provides case studies, which can be advantageous for engineers in guaranteeing the reliable integration of renewable energy sources into the power grid in a cost-efficient manner.

**Funding:** This research received no external funding.

**Institutional Review Board Statement:** Not applicable.

**Informed Consent Statement:** Not applicable.

**Data Availability Statement:** No new data were created or analyzed in this study. Data sharing is not applicable to this article.

**Conflicts of Interest:** The authors declare no conflict of interest.

## References

1. Carolinas Resource Plan Pathways and Core Portfolios. 2023. Available online: <https://starw1.ncuc.gov/NCUC/ViewFile.aspx?Id=0ae7fa49-ce8f-4df2-954d-0637b35e2f7b> (accessed on 6 June 2024).
2. Chapter NC Supplement: 2023–2024 Carbon Plan and Integrated Resource Plan Supplemental Planning Analysis. 2023. Available online: <https://starw1.ncuc.gov/NCUC/ViewFile.aspx?Id=1b85a555-3226-4f6a-907b-99dc0a30b09b> (accessed on 25 April 2024).
3. Nearly a Quarter of the Operating U.S. Coal-Fired Fleet Scheduled to Retire by 2029—U.S. Energy Information Administration (EIA). (n.d.). Available online: <https://www.eia.gov/todayinenergy/detail.php?id=54559> (accessed on 6 June 2024).
4. Elavarasan, R.; Shafiullah, G.; Padmanaban, S.; Kumar, N.; Annam, A.; Vetrichelvan, A.M.; Mihet-Popa, L.; Holm-Nielsen, J. A comprehensive review on renewable energy development, challenges, and policies of leading Indian states with an international perspective. *IEEE Access* **2020**, *8*, 74432–74457. [[CrossRef](#)]
5. Edianto, A.; Trencher, G.; Manych, N.; Matsubae, K. Forecasting coal power plant retirement ages and lock-in with random forest regression. *Patterns* **2023**, *4*, 100776. [[CrossRef](#)] [[PubMed](#)]
6. Li, D.; Zhang, Z.; Zhou, X.; Zhang, Z.; Yang, X. Cross-wind dynamic response of concrete-filled double-skin wind turbine towers: Theoretical modelling and experimental investigation. *J. Vib. Control*. **2023**. [[CrossRef](#)]
7. Saeed, M.; Fangzong, W.; Kalwar, B.; Iqbal, S. A Review on Microgrids' Challenges & Perspectives. *IEEE Access* **2021**, *9*, 166502–166517. [[CrossRef](#)]
8. Fan, L. *Control and Dynamics in Power Systems and Microgrids*; CRC Press: Boca Raton, FL, USA, 2017.
9. Chatterjee, S.; Chatterjee, S. Review on the techno-commercial aspects of wind energy conversion system. *IET Renew. Power Gener.* **2018**, *12*, 1581–1608. [[CrossRef](#)]
10. Santos-Ramos, J.E.; Saldarriaga-Zuluaga, S.D.; López-Lezama, J.M.; Muñoz-Galeano, N.; Villa-Acevedo, W.M. Microgrid Protection Coordination Considering Clustering and Metaheuristic Optimization. *Energies* **2024**, *17*, 210. [[CrossRef](#)]
11. Srivastava, A.; Mohanty, R.; Ghazvini, M.; Tuan, L.; Steen, D.; Carlson, O. A Review on Challenges and Solutions in Microgrid Protection. In Proceedings of the 2021 IEEE Madrid PowerTech, Madrid, Spain, 28 June–2 July 2021; pp. 1–6. [[CrossRef](#)]
12. Altaf, M.; Arif, M.; Islam, S.; Haque, M. Microgrid Protection Challenges and Mitigation Approaches—A Comprehensive Review. *IEEE Access* **2022**, *10*, 38895–38922. [[CrossRef](#)]
13. Li, Y.; Fan, L.; Miao, Z. Stability control for wind in weak grids. *IEEE Trans. Sustain. Energy* **2019**, *10*, 2094–2103. [[CrossRef](#)]
14. Lee, W.-G.; Nguyen, T.-T.; Yoo, H.J.; Kim, H.-M. Low-Voltage Ride-Through Operation of Grid-Connected Microgrid Using Consensus-Based Distributed Control. *Energies* **2018**, *11*, 2867. [[CrossRef](#)]
15. Heydari-Doostabad, H.; Khalghani, M.; Khooban, M. A novel control system design to improve LVRT capability of fixed speed wind turbines using STATCOM in presence of voltage fault. *Int. J. Elect. Power Energy Syst.* **2016**, *77*, 280–286. [[CrossRef](#)]
16. Liu, X.; Xu, Z.; Wong, K.P. Recent advancement on technical requirements for grid integration of wind power. *J. Mod. Power Syst. Clean Energy* **2013**, *1*, 212–218. [[CrossRef](#)]
17. Alaboudy, A.; Mahmoud, H.; Elbaset, A.; Abdelsattar, M. Technical Assessment of the Key LVRT Techniques for Grid-Connected DFIG Wind Turbines. *Arab. J. Sci. Eng.* **2023**, *48*, 15223–15239. [[CrossRef](#)]
18. Howlader, A.; Senjyu, T. A comprehensive review of low voltage ride through capability strategies for the wind energy conversion systems. *Renew. Sustain. Energy Rev.* **2016**, *56*, 643–658. [[CrossRef](#)]

19. Mehrdad, T.; Muttaqi, K. Low Voltage Ride Through of Wind Energy Systems. In *Reliable and Sustainable Electric Power and Energy Systems Management*; Springer: Singapore, 2017. [[CrossRef](#)]
20. Daravath, R.; Sandepudi, S.R. Low Voltage Ride Through Control Strategy for a Two-Stage Grid-Tied Solar Photovoltaic System with Grid Faults. *Electr. Power Compon. Syst.* **2024**, *1*–20. [[CrossRef](#)]
21. Mahela, O.; Gupta, N.; Khosravy, M.; Patel, N. Comprehensive Overview of Low Voltage Ride Through Methods of Grid Integrated Wind Generator. *IEEE Access* **2019**, *7*, 99299–99326. [[CrossRef](#)]
22. Mostafa, M.; El-Hay, E.; Elkholy, M. An overview and case study of recent low voltage ride through methods for wind energy conversion system. *Renew. Sustain. Energy Rev.* **2023**, *183*, 113521. [[CrossRef](#)]
23. Erlich, I.; Bachmann, U. Grid code requirements concerning connection and operation of wind turbines in Germany. In Proceedings of the IEEE Power Engineering Society General Meeting, Tampa, FL, USA, 16–17 June 2005; pp. 1253–1257.
24. Wu, Q. Grid Code Requirements for Wind Power Integration. In *Modeling and Modern Control of Wind Power*; IEEE: New York, NY, USA, 2018; pp. 11–36. [[CrossRef](#)]
25. Din, Z.; Zhang, J.; Zhu, Y.; Xu, Z.; El-Naggar, A. Impact of Grid Impedance on LVRT Performance of DFIG System with Rotor Crowbar Technology. *IEEE Access* **2019**, *7*, 127999–128008. [[CrossRef](#)]
26. Meegahapola, L.; Littler, T.; Flynn, D. Decoupled-DFIG fault ride-through strategy for enhanced stability performance during grid faults. *IEEE Trans. Sustain. Energy* **2010**, *1*, 152–162. [[CrossRef](#)]
27. Duong, M.; Sava, G.; Grimaccia, F.; Leva, S.; Mussetta, M.; Costinas, S.; Golovanov, N. Improved LVRT based on coordination control of active crowbar and reactive power for doubly fed induction generators. In Proceedings of the 9th International Symposium on Advanced Topics in Electrical Engineering (ATEE), Bucharest, Romania, 7–9 May 2015; pp. 650–655.
28. Saidi, Y.; Mezouar, A.; Benmahdjoub, M. A Comprehensive Review of LVRT Capability and Advanced Nonlinear Backstepping Control of Grid-Connected Wind-Turbine-Driven Permanent Magnet Synchronous Generator During Voltage Dips. *J. Control Autom. Electr. Syst.* **2022**, *33*, 1773–1791. [[CrossRef](#)]
29. Li, X.; Zhang, X.; Lin, Z.; Niu, Y. An Improved Flux Magnitude and Angle Control with LVRT Capability for DFIGs. *IEEE Trans. Power Syst.* **2018**, *33*, 3845–3853. [[CrossRef](#)]
30. Yuan, S.; Wei, Y.; Wei, Y.; Qi, H.; Gao, Y.; Qiao, J. Model Predictive Control Based PV Low Voltage Ride Through Strategy. In Proceedings of the 2021 IEEE International Conference on Predictive Control of Electrical Drives and Power Electronics (PRECEDE), Jinan, China, 20–22 November 2021; pp. 933–941. [[CrossRef](#)]
31. Mobarak, M.; Abdelrahem, M.; Stati, N.; Kennel, R. Model predictive control for low-voltage ride-through capability improvement of variable-speed wind energy conversion systems. In Proceedings of the 2016 International Symposium on Industrial Electronics (INDEL), Banja Luka, Bosnia and Herzegovina, 3–5 November 2016; pp. 1–6. [[CrossRef](#)]
32. Onishi, K.; Li, Y.; Koiwa, K.; Liu, F.; Zanma, T.; Liu, K. Analysis on the operation of crowbar in doubly fed induction generators. *Electr. Power Syst. Res.* **2023**, *215 Pt A*, 108950. [[CrossRef](#)]
33. Zhou, H.; Yang, G.; Li, D. Short circuit current analysis of DFIG wind turbines with crowbar protection. In Proceedings of the 2009 International Conference on Electrical Machines and Systems, Tokyo, Japan, 15–18 November 2009; pp. 1–6. [[CrossRef](#)]
34. Haidar, A.; Muttaqi, K.; Hagh, M. A Coordinated Control Approach for DC link and Rotor Crowbars to Improve Fault Ride-Through of DFIG-Based Wind Turbine. *IEEE Trans. Ind. Appl.* **2017**, *53*, 4073–4086. [[CrossRef](#)]
35. Yang, L.; He, J.; Yan, W.; Zhang, D.; Wu, X.; Huang, R.; Luo, Y.; Cai, G. Reactive Power Support Strategy for Low Voltage Ride Through Based on Sensitivity Analysis. In Proceedings of the 2021 IEEE 4th International Electrical and Energy Conference (CIEEC), Wuhan, China, 28–30 May 2021; pp. 1–8. [[CrossRef](#)]
36. Mohammed, N.; Zhou, W.; Bahrani, B. Impacts of the Reactive Power Control on the Small-signal Stability of Grid Forming Inverters. In Proceedings of the 2023 IEEE PES Innovative Smart Grid Technologies—Asia (ISGT Asia), Auckland, New Zealand, 21–24 November 2023; pp. 1–5. [[CrossRef](#)]
37. Pannell, G.; Zahawi, B.; Atkinson, D.; Missailidis, P. Evaluation of the Performance of a DC-Link Brake Chopper as a DFIG Low-Voltage Fault-Ride-Through Device. *IEEE Trans. Energy Convers.* **2013**, *28*, 535–542. [[CrossRef](#)]
38. Zhu, J.; Deng, Z.; Yu, L.; Li, S.; Qu, C.; Qiu, W.; Adam, G.P.; Booth, C. A DC chopper-based fast active power output reduction scheme for DFIG wind turbine generators. *IET Renew. Power Gener.* **2021**, *15*, 2480–2490. [[CrossRef](#)]
39. Hiremath, R.; Moger, T. Comprehensive review on low voltage ride through capability of wind turbine generators. *Int. Trans. Electr. Energy Syst.* **2020**, *30*, e12524. [[CrossRef](#)]
40. Ahmed, M.; Kandil, T.; Ahmed, E. Enhancing Doubly Fed Induction Generator Low-Voltage Ride-through Capability Using Dynamic Voltage Restorer with Adaptive Noise Cancellation Technique. *Sustainability* **2022**, *14*, 859. [[CrossRef](#)]
41. Khan, M.; Haque, A.; Kurukuru, V. Dynamic Voltage Support for Low-Voltage Ride-Through Operation in Single-Phase Grid-Connected Photovoltaic Systems. *IEEE Trans. Power Electron.* **2021**, *36*, 12102–12111. [[CrossRef](#)]
42. Lopez, J.; Sanchis, P.; Roboam, X.; Marroyo, L. Dynamic Behavior of the Doubly Fed Induction Generator During Three-Phase Voltage Dips. *IEEE Trans. Energy Convers.* **2007**, *22*, 709–717. [[CrossRef](#)]
43. Jia-hu, G.; Lu-hua, Z.; Xu, C. Dynamic response of wind power generation based on DFIG under grid fault. In Proceedings of the 2009 IEEE 6th International Power Electronics and Motion Control Conference, Wuhan, China, 17–20 May 2009; pp. 2275–2278. [[CrossRef](#)]
44. Li, B.; Liu, J.; Wang, X.; Zhao, L. Fault Studies and Distance Protection of Transmission Lines Connected to DFIG-Based Wind Farms. *Appl. Sci.* **2018**, *8*, 562. [[CrossRef](#)]

45. Lopez, J.; Gubia, E.; Olea, E.; Ruiz, J.; Marroyo, L. Ride Through of Wind Turbines with Doubly Fed Induction Generator Under Symmetrical Voltage Dips. *IEEE Trans. Ind. Electron.* **2009**, *56*, 4246–4254. [[CrossRef](#)]
46. Glover, J.; Sarma, M.; Overbye, T.; Birchfield, A. *Power System Analysis and Design*; Cengage Learning: Boston, MA, USA, 2016; ISBN 130588695X/9781305886957.
47. Ma, M.; Wang, W.; Wang, F.; Ren, X.; Wang, Z. Faulty Phase Recognition Method for Single-Line-to-Ground Fault in Resonant Grounded Distribution Networks. In Proceedings of the 2018 International Conference on Power System Technology (POWERCON), Guangzhou, China, 6–8 November 2018; pp. 351–357. [[CrossRef](#)]
48. Xin, S.; Li, Y.; Li, T.; Lu, Y. Single Phase Ground Fault Locating Method of Multi-Branch Wind Farm Collector Lines. In Proceedings of the 2021 IEEE 2nd China International Youth Conference on Electrical Engineering (CIYCEE), Chengdu, China, 15–17 December 2021; pp. 1–5. [[CrossRef](#)]

**Disclaimer/Publisher’s Note:** The statements, opinions and data contained in all publications are solely those of the individual author(s) and contributor(s) and not of MDPI and/or the editor(s). MDPI and/or the editor(s) disclaim responsibility for any injury to people or property resulting from any ideas, methods, instructions or products referred to in the content.